Nonlinear Wavefield Characteristics of Seismic Translation and Rotation in Small-Strain Deformation: Insights from Moment Tensor Simulations

Wei Li [1,2,], Yun Wang [1,2,*], Chang Chen[1,2], Lixia Sun[1,3]

[1] *"MWMC" group, School of Geophysics and Information Technology, China University of Geosciences, Beijing* 100083, *China*

[2] *State Key Laboratory of Geological Processes and Mineral Resources, China University of Geosciences, Beijing* 100083, *China*

[3] *Sinopec Research Institute of Petroleum Engineering Co., Ltd., Beijing* 102206, *China*

[*] Corresponding author: wangyun@mail.gyig.ac.cn.

Abstract Seismic rotational motions recorded in near-field and strong-magnitude observations exhibit discrepancies with theoretical predictions derived from linear elastodynamic principles. To explore potential nonlinear contributions to the phenomenon, this study incorporates nonlinear strain effects into wave propagation theory through Green-Lagrange strain tensor formulations. A staggered-grid finite-difference method simulates six-component wavefields (translational and rotational) generated by three fundamental seismic sources: isotropic (ISO), double-couple (DC), and compensated linear vector dipole (CLVD). Results demonstrate that nonlinear effects strongly depend on source characteristics and energy intensity. ISO sources exhibit uniform nonlinear anomalies from

23 volumetric-shear coupling, CLVD sources amplify directional strain-axis effects, and

24 DC sources amplify localized nonlinearity along faulting directions. Rotational

25 components show higher sensitivity to nonlinearity than translational components,

26 which are also contingent on source-receiver geometry. Simulations of two

27 moderate-strong earthquakes highlight surface waves as preferential carriers of

28 nonlinear signatures, though path effects and site amplification require systematic

29 exploration. These results establish a framework for advancing nonlinearity study in

30 ground motion analysis while emphasizing the need for instrumentally resolved

31 rotational measurements and complex media modeling.

32

33 **1 Introduction**

34   Seismic rotational motions can be recorded in ground shaking, especially when

35 caused by strong earthquakes (Graizer, 1991; 2010; Zhou et al., 2019). These

36 rotational motions exhibit pronounced characteristics in shallow focal depths and

37 near-field conditions (Kozak, 2009; Sun et al., 2017). Within the domain of structural

38 engineering, the incorporation of rotational analysis has gained increasing recognition

39 for its critical role in assessing ground motion stability and building design (Li, 1991;

40 Li and Sun, 2001; Yan, 2017; Huras et al., 2021). Studies advancements suggest that

41 incorporating seismic rotation data, which captures spatial gradients, can enhance the

42 accuracy of earthquake source characterization and moment tensor inversion

43 (Bernauer et al., 2014; Donner, 2016; Ichinose et al., 2021), as supported by

44 simulations conducted by Hua and Zhang (2022).

45   The work of Lee (2007) comprehensively reviewed the applications of seismic

46 rotation observations in seismic engineering, postulating that the measured rotation

47 components in strong ground motion predominantly originate from the nonlinear

48 elasticity and site effect. This conclusion is drawn from empirical evidence showing

49 that actual rotational measurements exceed derived rotational components from

50 translational data by 1-2 orders of magnitude. In addressing the complex geophysical

51 phenomena stemming from Earth's heterogeneities, progress has been made in

52 developing analytical solutions for nonlinear wave equations through iterative

53 techniques in Green's function (McCall, 1994). Notable methodological developments

54 include the flux-corrected transport method (Yang et al., 2002; Zheng et al., 2006) and

55 perturbation approaches (Bataille and Contreras, 2009; Jia et al., 2020), which have

56 been instrumental in investigating nonlinear effects on elastic wave propagation.

57 However, current studies primarily focus on nonlinear constitutive relations between

58 stress and strain under small strain and its linearization approximations (Renaud et al.,

59 2012; 2013; TenCate et al., 2016; Feng et al., 2018), leaving a gap in understanding

60 the strain nonlinearity. This aspect may hold the key to more accurate representations

61 of rotational motions in strong earthquakes and near-field conditions.

62 In the seismically active region of Taiwan, broadband seismic observations and

63 physical source studies have revealed significant rotational components in Taiwan's

64 seismic events, demonstrating distinct strike-slip rotation characteristics between the

65 southern and northern regions of the island (Yu et al., 1999; Wang and Lv, 2006).

66 Oliveira and Bolt (1989) estimated rotational components of strong motions,

67 confirming their non-negligible impact in near-field observations across Taiwan.

68 Through analysis of six-component ground motion data from 52 earthquakes recorded

69 at the HGSD station in eastern Taiwan during 2007-2008, Chen et al. (2014)

70 identified substantial vertical rotational motions in proximal seismic locations and

71 notable differences in energy and spectral characteristics between horizontal and

72 vertical rotational motions. These studies show the importance of seismic rotation

73 analysis in elucidating Taiwan's subsurface structures and geodynamic processes.

74 In this research, we develop a theoretical and numerical framework for analyzing

75 nonlinear seismic wave propagation through Green strain tensor formulations. We

76 derive velocity-stress equations incorporating nonlinear strain coupling terms, employ

77 a staggered-grid finite-difference method to simulate six-component wavefields, and

78 examine nonlinear six-component (C) wavefield characteristics through numerical

79 simulations of three fundamental seismic moment tensor sources. Additionally, we

80 conduct theoretical simulations of focal mechanisms of near-field and strong

81 earthquakes along the Taiwan coast, analyzing source-dependent nonlinear responses

82 to establish foundational insights for guiding future observational data studies.

83 **2 Theory and method**

84 2.1 Elastodynamic theory

85 Consider an elastic medium in three-dimensional space under orthogonal

86 Cartesian coordinate (Fig. 1). Let particle A at position **x** within the medium, with an

87 adjacent particle B at **x**+d**x**. The infinitesimal line element connecting these particles

88 has an initial length ds. When subjected to external force, the material element AB

89 undergoes displacement $u(x, t)$, transitioning to new positions A' and B' at **x**' and

90 **x**'+d**x**', respectively, with a deformed length ds'. This deformation comprises both

91 rigid-body displacement and strain-induced distortion. The work performed by the

92 external force manifests as kinetic energy from particle motion and potential energy

93 stored through elastic deformation. The strain energy density can be quantified by the

94 differential quadratic form of the line element's length variation given in Eq. (1).
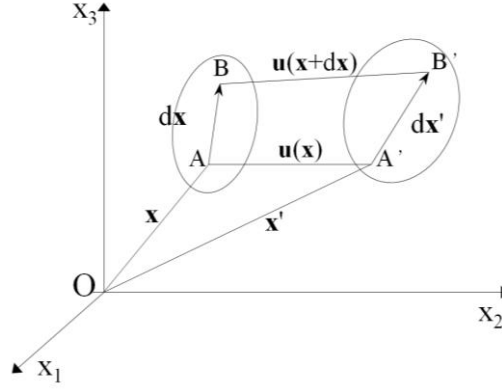
95

Figure 1. Schematic diagram of displacement and deformation of an elastic medium

(Adapted from Aki and Richards (2002))

$$(ds')^2 - (ds)^2 = 2E_{ij}dx_i dx_j, \ i, j \in \{1,2,3\} \tag{1}$$

where E_{ij} denotes the Green-Lagrange strain tensor components. All tensor equations

adhere to the Einstein summation convention with dummy index notation. The

displacement field u_i in Cartesian coordinate x_j defines the Green strain tensor (Eq.

(2)), which provides an objective measure of deformation before and after external

force application

$$E_{ij} = \frac{1}{2}(\frac{\partial u_j}{\partial x_i} + \frac{\partial u_i}{\partial x_j} + \frac{\partial u_k}{\partial x_i} \cdot \frac{\partial u_k}{\partial x_j}), \ i, j, k \in \{1,2,3\} \tag{2}$$

The displacement gradient tensor decomposes into symmetric strain (e_{ij}) and

antisymmetric rotation (r_{ij}) components:

$$\frac{\partial u_j}{\partial x_i} = e_{ij} + r_{ij} \tag{3}$$

$$e_{ij} = \frac{1}{2}(\frac{\partial u_j}{\partial x_i} + \frac{\partial u_i}{\partial x_j}), \ r_{ij} = \frac{1}{2}(\frac{\partial u_i}{\partial x_j} - \frac{\partial u_j}{\partial x_i}) \tag{4}$$

Conventional elastodynamic theory linearizes the Green strain tensor by neglecting

second-order displacement gradient terms ($\partial u_k/x_i \, \partial u_k/x_j$), reducing it to the

infinitesimal strain approximation:

112
$$E_{ij} \approx e_{ij} = \frac{1}{2}(\frac{\partial u_j}{\partial x_i} + \frac{\partial u_i}{\partial x_j}), \ i,j \in \{1,2,3\} \tag{5}$$

113   For isotropic elastic materials, the strain-stress relationship is given by:

114
$$\sigma_{ij} = \lambda \delta_{ij} e_{kk} + 2\mu e_{ij}, \ i,j,k \in \{1,2,3\} \tag{6}$$

115   where λ and μ are Lamé coefficients, and δ_{ij} is the Kronecker delta. Incorporating

116   nonlinearity through the complete Green strain tensor yields:

117
$$\sigma_{ij} = \lambda \delta_{ij} E_{kk} + 2\mu E_{ij}$$
$$= \lambda \delta_{ij} e_{kk} + 2\mu e_{ij} + \underbrace{\frac{1}{2}\lambda \delta_{ij}(\frac{\partial u_k}{\partial x_m}\cdot\frac{\partial u_k}{\partial x_m}) + \mu \frac{\partial u_k}{\partial x_i}\cdot\frac{\partial u_k}{\partial x_j}}_{\text{additional terms}}, \ i,j,k,m \in \{1,2,3\} \tag{7}$$

118   Substituting the nonlinear constitutive relation (Eq. (7)) into the momentum

119   conservation law (Eq. (8)), where ρ is the material density.

120
$$\rho\frac{\partial^2 u_i}{\partial t^2} = \frac{\partial \sigma_{ij}}{\partial x_j}, \ i,j \in \{1,2,3\} \tag{8}$$

121   Yields the nonlinear wave equation:

122
$$\rho\frac{\partial^2 u_i}{\partial t^2} = \frac{\partial}{\partial x_j}\left(\lambda \delta_{ij} E_{kk} + 2\mu E_{ij}\right)$$
$$= \underbrace{(\lambda+\mu)\frac{\partial^2 u_j}{\partial x_i \partial x_j} + \mu\frac{\partial^2 u_i}{\partial x_j \partial x_j}}_{\text{original terms}} + \underbrace{\lambda\frac{\partial u_k}{\partial x_i}\frac{\partial^2 u_k}{\partial x_j x_j} + \mu\left(\frac{\partial^2 u_k}{\partial x_i x_j}\frac{\partial u_k}{\partial x_j} + \frac{\partial^2 u_k}{\partial x_j x_j}\frac{\partial u_k}{\partial x_i}\right)}_{\text{additional terms}}, \ i,j,k \in \{1,2,3\} \tag{9}$$

123   In Eq. (9), the original terms correspond to the classical linear wave equation,

124   while the additional terms arise from the nonlinear strain contributions. This reveals

125   two fundamental nonlinear effects: (i) Volumetric nonlinearity (associated with λ):

126   Coupling between shear deformation and volumetric strain. (ii) Shear nonlinearity

127   (associated with μ): Interdependence of shear stress and principal strains. These

128   additional third-order terms introduce complex interactions between deformation

129   modes that are absent in linear theory. Their seismic manifestations depend critically

130   on material properties and source characteristics, necessitating targeted numerical

131   simulations to quantify nonlinear effects on wave propagation.

132   2.2 Staggered-grid finite-difference method

133   The staggered-grid finite-difference (SGFD) technique has proven effective for

134   simulating seismic wave propagation. This method employs dual grid systems to

135   discretize velocity-stress formulations, enabling stable computation of wavefield

136   evolution in discrete spatial-temporal domains (Madariaga, 1976; Sun et al., 2018). As

137   illustrated in Fig. 2, stress and velocity components are distributed across offset grid

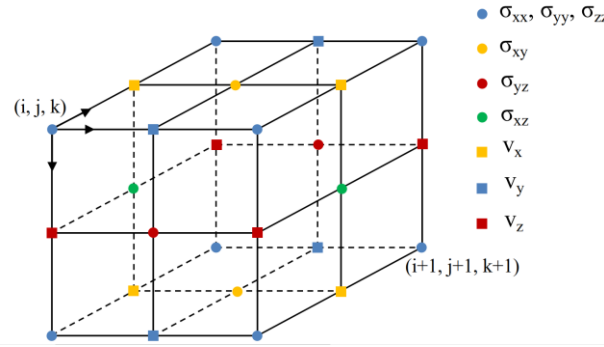138   points to optimize numerical accuracy.

139

140   **Figure 2.** 3D staggered-grid configuration for velocity-stress formulations.

141   For 3D elastic isotropic media, we extend conventional linear strain formulations

142   (Pei, 2005) by incorporating the nonlinear strain tensor E_{ij}. Temporal differentiation of

143   the constitutive relation(Eq.(7)) yields velocity-stress relationships when combined

144   with Eq. (8).

8

145
$$\begin{cases} \rho \dfrac{\partial v_i}{\partial t} = \dfrac{\partial \sigma_{ij}}{\partial x_j} \\[2mm] \dfrac{\partial \sigma_{ij}}{\partial t} = \lambda \delta_{ij} \dfrac{\partial E_{kk}}{\partial t} + 2\mu \dfrac{\partial E_{ij}}{\partial t} \\[2mm] \qquad = \lambda \delta_{ij} \dfrac{\partial v_k}{\partial x_k} + \mu(\dfrac{\partial v_i}{\partial x_j} + \dfrac{\partial v_j}{\partial x_i}) + \underbrace{\lambda \delta_{ij}(\dfrac{\partial v_k}{\partial x_m} \cdot \dfrac{\partial u_k}{\partial x_m}) + 2\mu \dfrac{\partial v_k}{\partial x_i} \cdot \dfrac{\partial u_k}{\partial x_j}}_{\text{additional terms}} \end{cases} \qquad , i,j,k,m \in \{1,2,3\} \quad (10)$$

146 where $v_i = \partial u_i/\partial t$($i \in \{x,\ y,\ z\}$). Nonlinear contributions emerge through

147 velocity-displacement coupling, whereupon take the displacement-preserving terms

148 (u_i) as products of velocity components v_i and time dt (serve as time step in

149 simulations) in the equations. In addition, rotation rates around Cartesian axes are

150 derived from the antisymmetric rotation tensor (Eq. (4)).

151 Based on the equations, we implement these formulations through C/C++ code

152 to numerically simulate seismic wave propagation. It contains perfectly matched layer

153 (PML) boundary to suppress boundary reflections (Dong and Ma, 2000) and acoustic

154 boundary replacement (Eq. (13)) for free-surface implementation (Xu et al., 2007;

155 Wang et al., 2012).

156
$$\begin{cases} \sigma^0_{zz} = 0 \\ \rho = 0.5\rho_0 \\ \lambda = 0 \\ \mu = \mu_0 \end{cases} \qquad (11)$$

157 where σ^0_{zz}, ρ, λ, and μ denote normal stress, medium density, and Lamé coefficients at

158 and above the free surface, while ρ_0 and μ_0 represent density and Lamé coefficients

159 below the free surface, respectively.

160 **3 Simulations of basic seismic moment sources**

161   3.1 Forward modelling parameters

162   Seismic moment tensors provide the most complete mathematical representation

163   of point sources when the seismic wavelength exceeds the source dimension (Gilbert,

164   1970). As defined in Eq. (12), the symmetric second-order moment tensor **M**

165   quantifies the equivalent force system acting at the hypocenter:

166    $$M_{ij} = \mu A(v_i n_j + v_j n_i), \ i, j \in \{1, 2, 3\} \tag{12}$$

167   Where μ is the shear modulus, A the fault area, v_i the slip vector, and n_j the fault

168   normal vector. The tensor can be decomposed into three fundamental components:

169   isotropy (ISO) component, double couple (DC) component, and compensated linear

170   vector dipole (CLVD) component (Knopoff and Randall, 1970; Jost and Hermann,

171   1989). Specifically, the ISO component represents volumetric change with non-zero

172   trace and uniform force along principal axes. The DC component signifies pure shear

173   dislocation without volumetric change without volume variation. The CLVD

174   component describes axial contraction/expansion with a dipole magnitude ratio

175   2:−1:−1. These moment tensor expressions can be written as Eq. (13). These

176   components govern distinct radiation patterns critical for understanding nonlinear

177   seismic wave propagation effects.

178    $$\boldsymbol{M}^{ISO} = \begin{pmatrix} M_{11} & 0 & 0 \\ 0 & M_{22} & 0 \\ 0 & 0 & M_{33} \end{pmatrix}, \boldsymbol{M}^{DC} = \begin{pmatrix} 0 & M_{12} & 0 \\ M_{21} & 0 & 0 \\ 0 & 0 & 0 \end{pmatrix}, \boldsymbol{M}^{CLVD} = \begin{pmatrix} M_{11} & 0 & 0 \\ 0 & M_{22} & 0 \\ 0 & 0 & -2M_{33} \end{pmatrix} \tag{13}$$

179   Following Graves(1996), we implement moment tensor sources in the

180   staggered-grid finite-difference scheme by converting body force to equivalent

181   velocity sources. The loading equations for the three moment sources are shown in Eq.

182   (14).

$$\boldsymbol{M}^{ISO}: \Delta v_i^n = \frac{M_{ij} \cdot dt \cdot f^n}{\rho V} \cdot \frac{\partial}{\partial x_j}$$

183
$$\boldsymbol{M}^{DC}: \Delta v_i^n = \frac{M_{jk} \cdot dt \cdot f^n}{\rho V} \cdot (\delta_{ij} \frac{\partial}{\partial x_k} + \delta_{ik} \frac{\partial}{\partial x_j})$$
(14)

$$\boldsymbol{M}^{CLVD}: \Delta v_i^n = \frac{M_{kl} \cdot dt \cdot f^n}{\rho V} \cdot (\delta_{ik} \frac{\partial}{\partial x_l} + \delta_{il} \frac{\partial}{\partial x_k} - \frac{2}{3} \delta_{kl} \frac{\partial}{\partial x_i})$$

184 where i, j, k, $l \in \{1,2,3\}$. Δv denotes velocity increment, n the time step index, dt the

185 time interval, ρ material density, and V grid cell volume. The source-time function f^n

186 uses a Ricker wavelet with amplitude at $n\ dt$.

187 To exclude effects on nonlinear wave propagation from complex medium

188 characteristics, we currently focus exclusively on simulations in a 3D homogeneous

189 isotropic full-space model. The numerical implementation employs the Ricker

190 wavelet with a 0.5 Hz dominant frequency. The model spans 80 km (x) $\times$ 80 km (y) $\times$

191 80 km (z) with a uniform grid spacing of 500 meters in X, Y, and Z directions.

192 Material properties are: P-wave velocity v_p=4400 m/s, S-wave velocity v_s=3000 m/s,

193 and density ρ=2600 kg/m^3. The source resides at the model center (40 km, 40 km, 40

194 km). Temporal discretization uses $\Delta t = 15$ ms, with second-order differential accuracy

195 in time and sixth-order in space.

196 For Numerical stability, based on the simulation parameters, the spatial

197 discretization achieves 10.4 ($v_s/\Delta/f_{dominant}$) points per wavelength for the dominant

198 frequency, which exceeds the 8–10 PPW threshold for sixth-order schemes to

199 suppress numerical dispersion artifacts (Virieux, 1986). Follows the temporal stability

200 of 3D Courant-Friedrichs-Lewy (CFL) criterion ($\Delta t \cdot v_{max} \cdot sqrt(1/\Delta x^2 + 1/\Delta y^2 + 1/\Delta z^2)$), it

201 reaches about 0.16. The resultant CFL number is a conservative value relative to the

202 empirical 3D stability limit of 0.5 (Moczo et al., 2007), ensuring waveform fidelity

203   while accommodating potential nonlinear term amplification.

204   3.2 Simulation results

205   3.2.1 ISO source

206   Fig. 3a displays 6C wavefield snapshots at 8 seconds for the ISO source under

207   nonlinear deformation condition. Translational components exhibit uniform P-wave

208   amplitudes, while rotational components show near absence of P-wave energy. The

209   wavefield differences between linear and nonlinear simulations (Fig.3b) reveal

210   emergent S-wave signatures, contrasting with classical elastodynamic theory, where

211   ISO sources exclusively generate P-waves in homogeneous isotropic media through

212   pure compressional/expansional volume change. The anomalous P-S coupling

213   phenomenon arises from nonlinear volumetric-shear strain interactions governed by

214   the constitutive relationship (Eq. (7)), where the higher-order terms enable energy

215   transfer between compressional and shear deformation modes.

216   Fig. 4 quantified the relative change between linear and nonlinear simulations at

217   each grid cell volume. We applied a stability threshold to the relative change

218   calculations to mitigate the influence of unrealistic wavefields (value$_{linear} \rightarrow 0$). It can

219   be seen from Fig.4 that (i) the spatial distribution exhibits general symmetry and

220   homogeneity with alternating positive/negative anomalies (Fig. 4a), where negative

221   values (<0) indicate overestimation by linear theory and positive values (>0) suggest

222   underestimation; (ii) rotational components have different and more complex

223   azimuthal distribution and larger relative changes than translational components, also

224   evidenced by probability density function (PDF) distributions in (Fig. 4b).
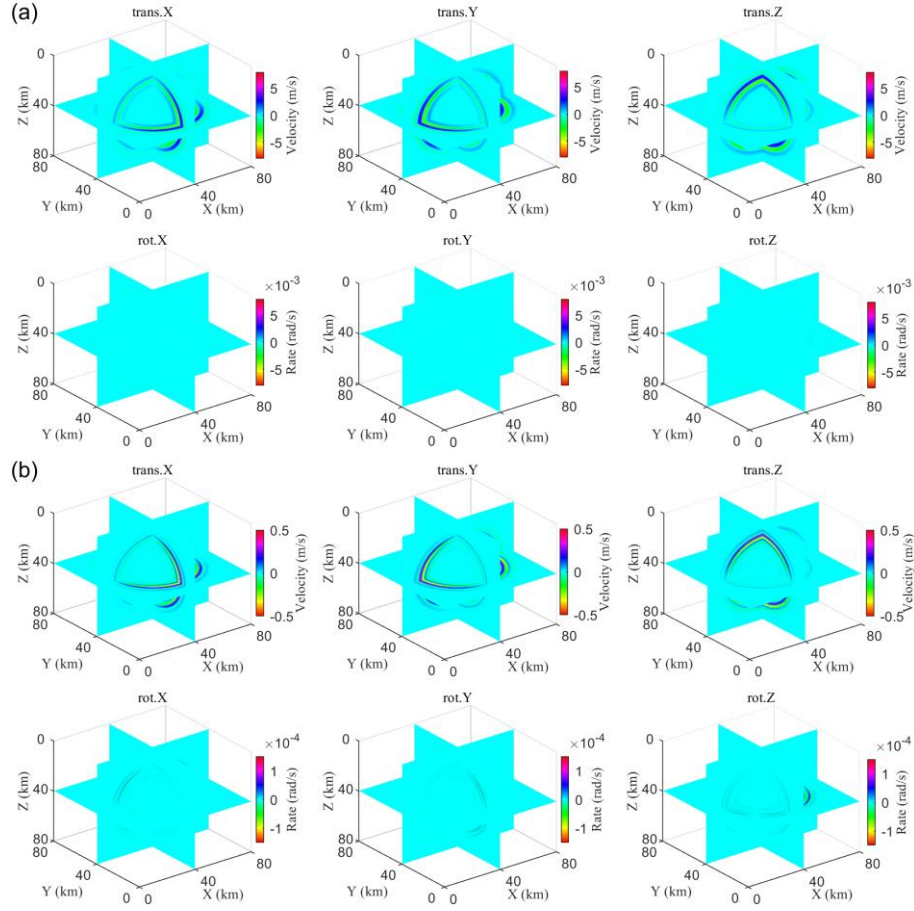
225

226

227   **Figure 3.** (a) Nonlinear 6C wavefield and (b) linear-nonlinear discrepancy for Mw7

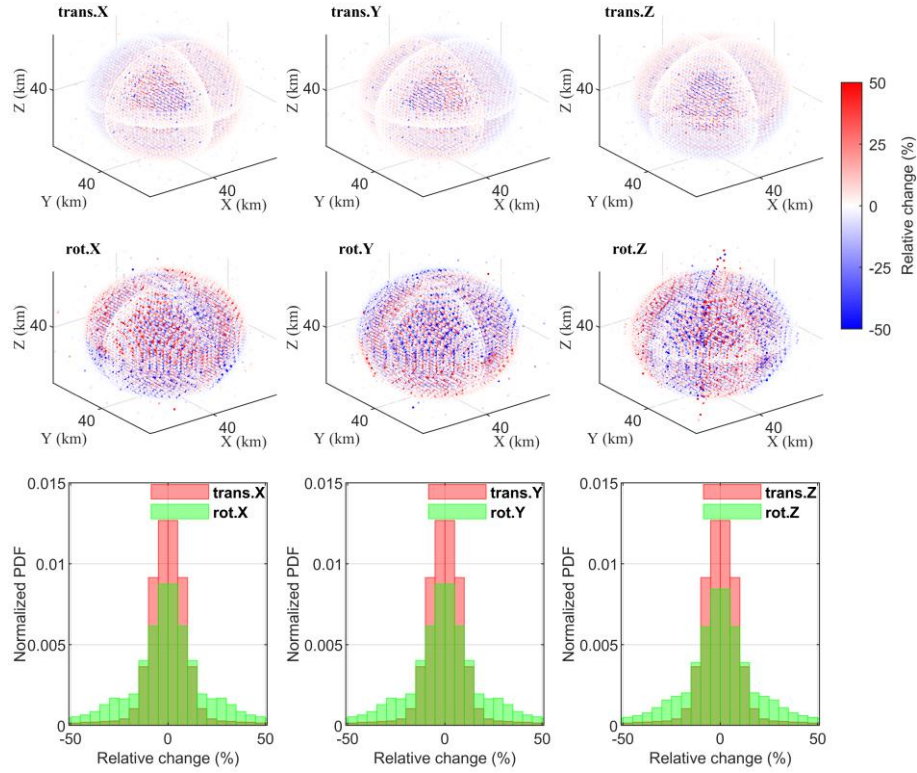228   ISO source at t=8s.

Figure 4. ISO source linear-nonlinear relative change: (a) 3D spatial distribution (b) Probability density function.

3.2.2 DC source

Fig. 5a presents 6C wavefield snapshots for the DC source under nonlinear conditions. The wavefield difference between nonlinear and linear wavefields in Fig. 5b demonstrates a different wavefront energy distribution from the original wavefront distribution in Fig. 5a. This energy redistribution caused by nonlinearity indicates that shear-dominated sources induce more complex nonlinear interactions.

The relative changes of nonlinear effects (Fig. 6) reveal not only zone variation but also localized strong nonlinearities at axial positions related to the distribution of the force couples tied to the DC source of fault displacement directions. At the same time, rotational components show a similar spatial distribution of underestimated and

242   overestimated areas and localized strong nonlinearities, and rot.X and rot.Y

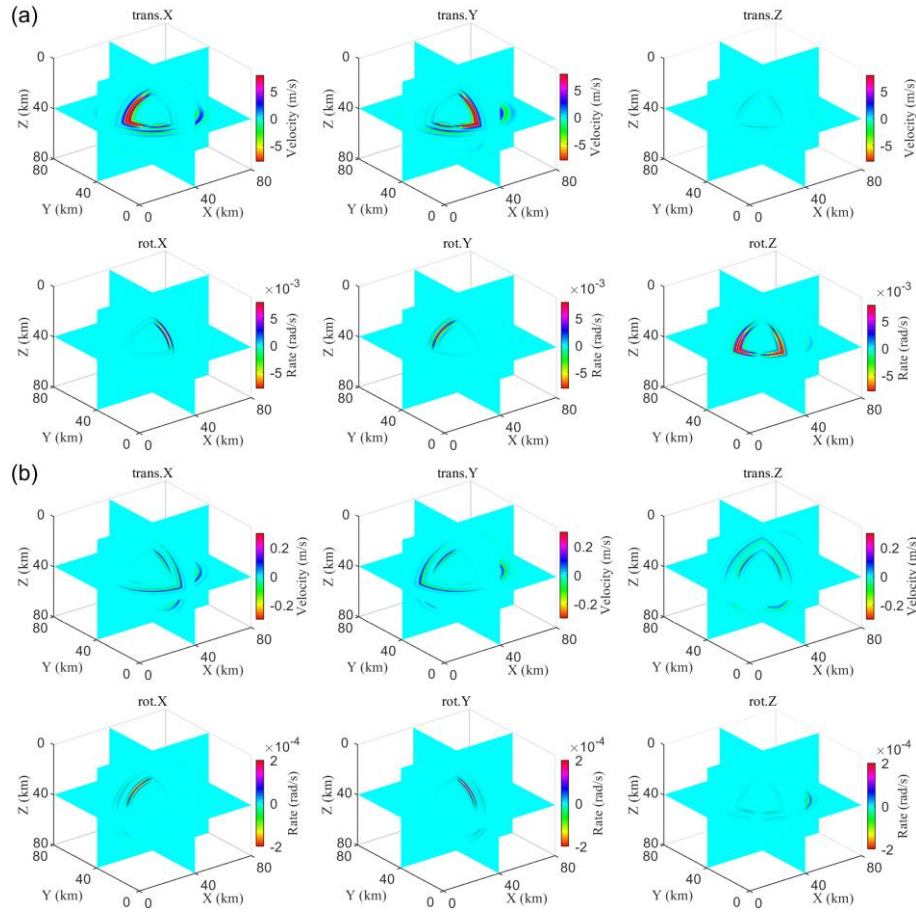243   components show larger change values, as seen from the PDF results.

244

245

246   **Figure 5.** (a) Nonlinear 6C wavefield and (b) linear-nonlinear discrepancy for

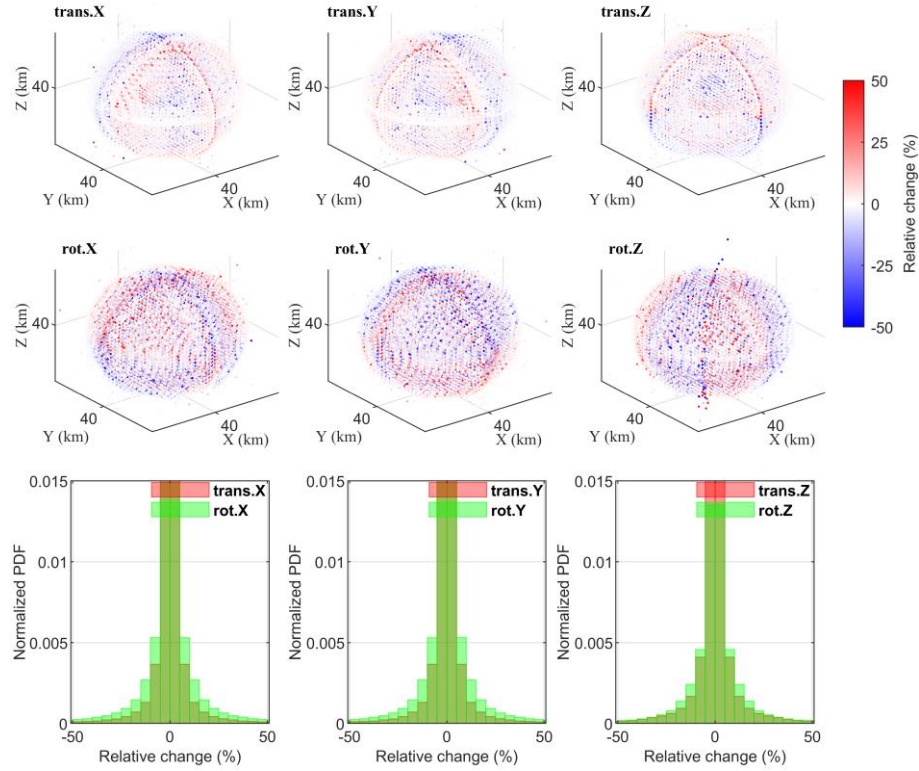247   Mw7 DC source at t=8s.

Figure 6. DC source linear-nonlinear relative change: (a) 3D spatial distribution (b) Probability density function.

3.2.3 CLVD source

Figs. 7 displays the results for the CLVD source simulation, demonstrating S-waves dominance in rotational components and its linear-nonlinear discrepancy in Fig. 7b highly resembles DC source results (Fig. 5b), reflecting their shared wavefield differences caused by nonlinearity for CLVD and DC source simulations may emerge from their fundamental kinematic similarity as non-volumetric source mechanisms.

Fig. 8 demonstrates Z-axis aligned anomalies corresponding to the CLVD compression axis for translational and rotational components, while the PDF distributions show overall enhanced nonlinear responses in rotational components.

261   The observed patterns correlate with the used CLVD source mechanism's kinematic

262   characteristics ─ axial compression of twice the force along Z and extension in x/y

263   directions ─ demonstrating how nonlinear effects inherit source radiation features
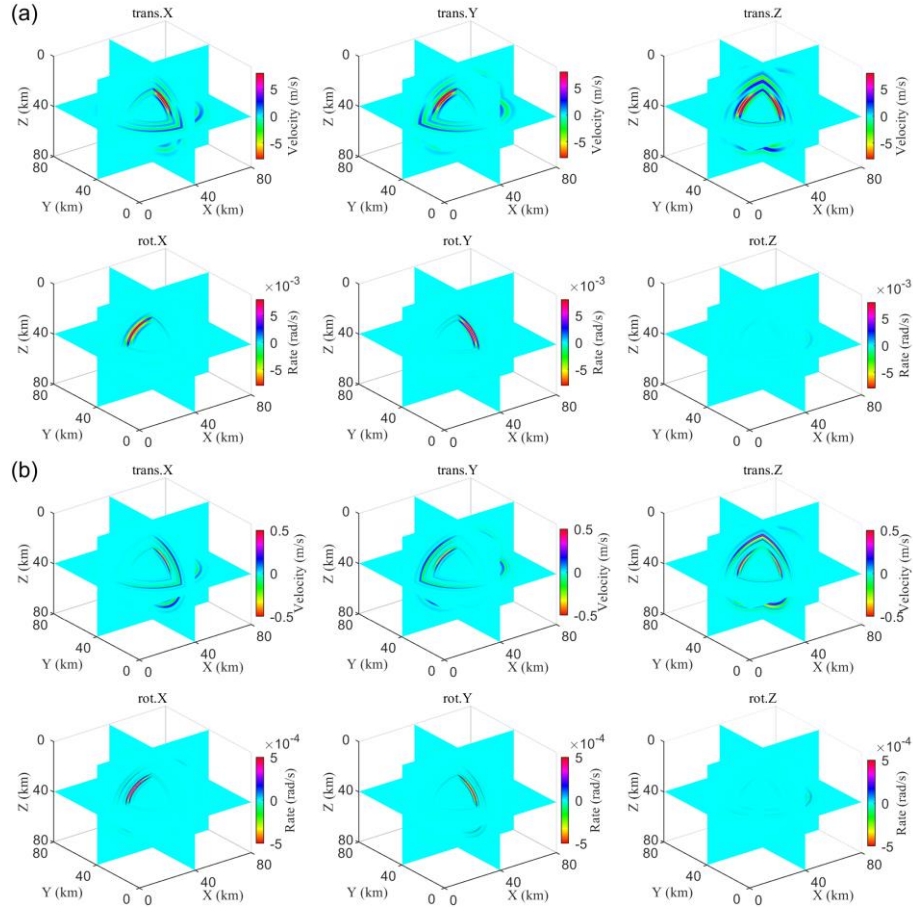
264   while introducing directional dependence.

265

266

267   **Figure 7.** (a) Nonlinear 6C wavefield and (b) linear-nonlinear discrepancy for Mw7

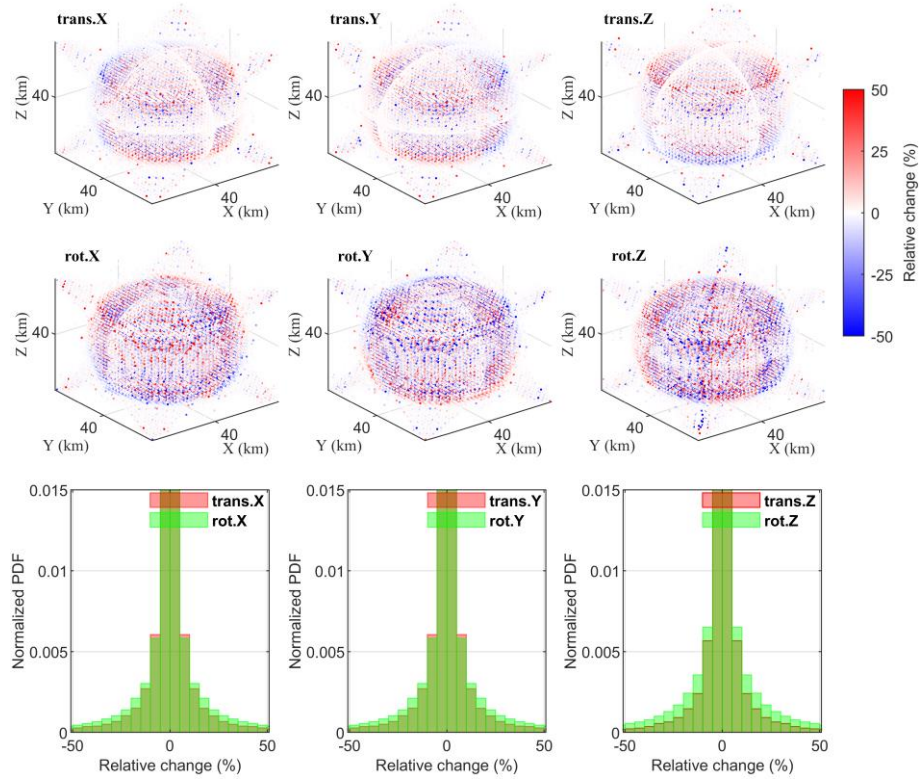268   CLVD source at t=8s.

Figure 8. CLVD source linear-nonlinear relative change: (a) 3D spatial distribution (b) Probability density function.

The three force source types exhibit distinct nonlinear signatures governed by their fundamental characteristics. ISO sources generate more homogeneous spatial nonlinear effects. CLVD sources amplify directional nonlinear anomalies along principal strain axes. DC sources primarily restrict local stronger nonlinear effects to the force-couple axis. These differences emerge from how each source type interacts with the nonlinear strain tensor in Eq. (2). The cross-term $1/2\ \partial u_k/\partial u_i \cdot \partial u_k/\partial u_j$ enables energy transfer between deformation modes and violates the linear theory's strict P-S decoupling. Rotational components demonstrate particular sensitivity to these higher-order interactions, as evidenced by their broader PDF distributions across all source types. This source-dependent nonlinear behavior underscores the importance

282   of considering rotational wavefield components and source kinematics when

283   interpreting strong ground motions.

284   3.3 Wavefield comparisons

285   The nonlinear effects on seismic wavefields are qualified through relative energy

286   change (ΔE) throughout the entire simulation domain using Eq. (15) and the

287   sensitivity ratio of rotational to translational ($\Delta E_{rot}/\Delta E_{trans}$).

288
$$\Delta E = \frac{E_{nonlinear} - E_{linnear}}{E_{linnear}} \times 100\% \,, \ E = \sum_{i,j,k} v_{i,j,k}^2 \Delta V \qquad (15)$$

289   where $v_{i,j,k}$ is wavefield value at each grid point and ΔV is unit grid cell volume.

290   Fig. 9 illustrates the global energy variations between nonlinear and linear

291   simulations at 6th seconds for ISO, CLVD, and DC sources. As the magnitude

292   increases, the relative change of global wavefield energy shows an exponential

293   increase, with sufficiently larger values of relative change when it reaches Mw 5. The

294   ISO source exhibits the most pronounced nonlinear effects, with relative energy

295   changes reaching 10.03% (translational) and 22.87% (rotational) at Mw7 (Fig. 9a,

296   Table 1). This contrasts with CLVD and DC sources showing smaller changes (CLVD:

297   3.64% translational, 6.41% rotational; DC: <1% in all components).

298   The ISO source introduces uniform energy amplification in seismic components

299   through nonlinear dilatational enhancing strain accumulation. The CLVD and DC

300   sources redistribute localized energy, suppressing net energy changes, especially for
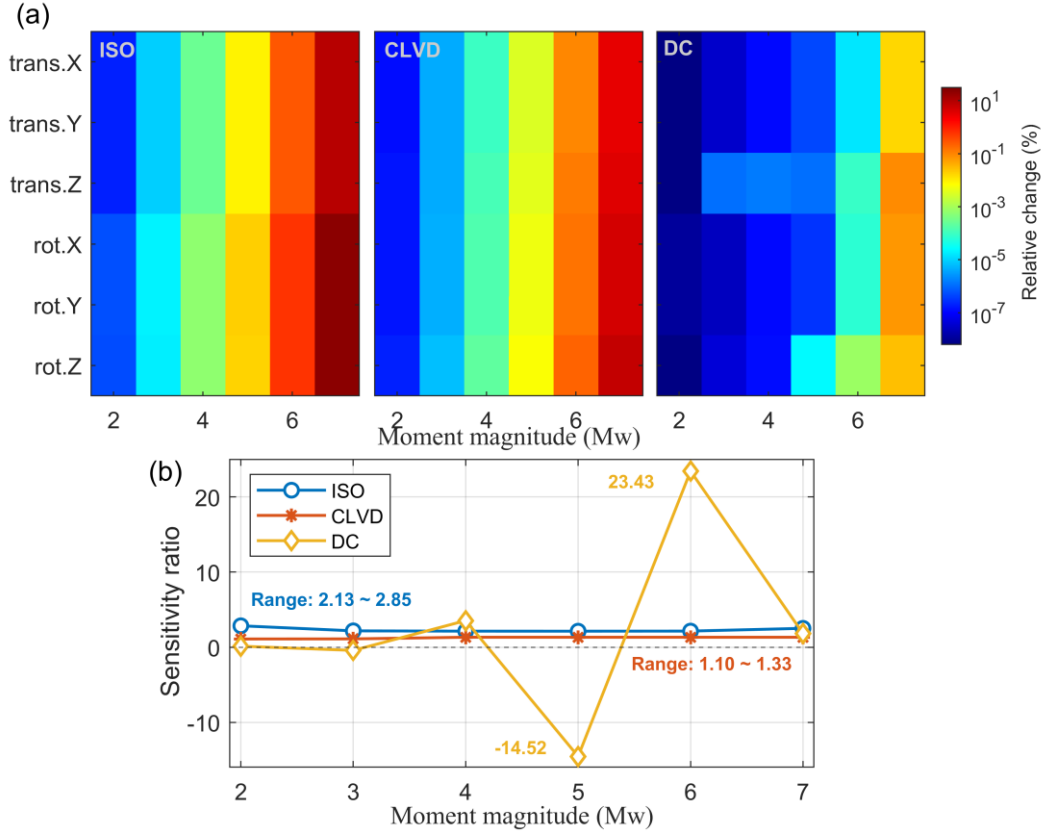
301   the DC source.

Figure 9. Relative energy changes induced by nonlinearity of (a) the three seismic sources at 6th second with increasing moment magnitude and sensitivity ratio of rotation vs. translation.

Table 1. Global wavefield energy change characteristics.

Source type	Max ΔE_{trans} (%, Mw7)	Max ΔE_{rot} (%, Mw7)	Sensitivity (rot./trans.)
ISO	10.03 (trans.)	22.87 (rot.)	2.13 ~ 2.85
CLVD	3.64 (trans.Z)	6.41 (rot.Z)	1.10 ~ 1.33
DC	0.03 (trans.Z)	0.09 (rot.Z)	extremes: -14.52, 23.43

The simulation results demonstrate that rotational measurements enhance nonlinear detection capability by 1-3× compared to traditional translational components. Current broadband seismometers possess sufficient resolution to detect these nonlinear wavefield anomalies. However, two critical constraints govern actual observational feasibility: magnitude-distance threshold and small/distant event

313   challenges.

314   Pronounced nonlinear signatures manifest primarily in large-magnitude events

315   (Mw ≥5) within near-field distances (simulated 30 km). This arises from strain

316   amplitudes exceeding 10^{-4}—the empirical threshold for detectable nonlinear coupling

317   (Guyer and Johnson, 1999), and limited geometric spreading and attenuation in

318   proximal regions. For smaller magnitudes (Mw <5) or far-field observations,

319   nonlinear strain amplitudes decay below, obscured by ambient noise floors, and path

320   effects (scattering, attenuation) and source radiation patterns disperse nonlinear

321   signatures. Given current instrumental limits (e.g., rotational sensor of a self-noise up

322   to $2 \times 10^{-8}\ rad/s/\sqrt{Hz}$), targeted studies of near-field and moderate to strong

323   earthquakes offer the most viable pathway to characterize nonlinear constitutive laws.

324   **4 Earthquakes simulations**

325   Building upon the theoretical framework for fundamental source types, we extend

326   our simulations to more complex scenarios incorporating realistic source mechanisms

327   and layered media. Analyzing two moderate-magnitude earthquakes (E1: Mw5.4 and

328   E2: Mw6.1) along the Taiwan coast aims to validate theoretical predictions of

329   nonlinear wave propagation and establish baseline understanding for future

330   observational comparisons. The events were respectively recorded at stations NA01

331   (E1) and QS01 (E2) (Chen et al., 2023), as shown in Fig. 10, depicted by GMT

332   (Wessel et al., 2019). Moment tensor solutions derived from the U.S. Geological

333   Survey (USGS) are defined in Eq. (16), with synthetic 6C seismograms generated

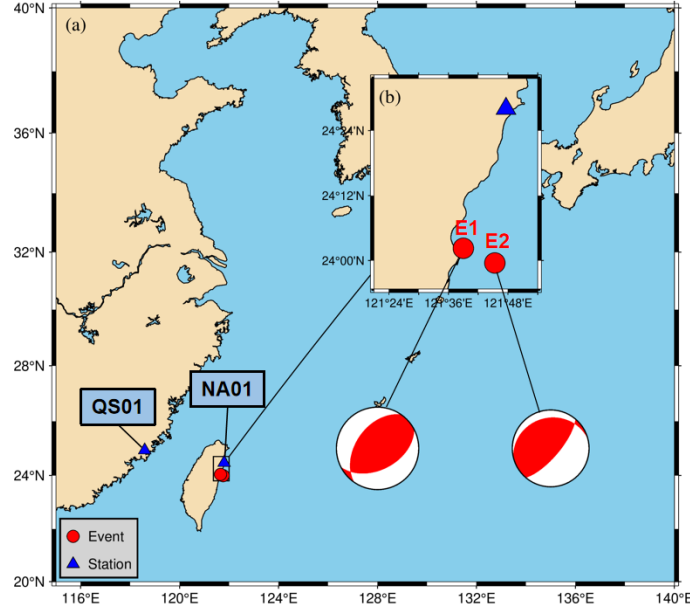334   under both linear and nonlinear constitutive relations.

335

336   **Figure 10.** Epicenters and observation sites of E1 and E2

$$E1:\begin{bmatrix} M_{xx} = -7.569 \times 10^{16}, M_{yy} = -2.373 \times 10^{16}, M_{zz} = 9.942 \times 10^{16} \\ M_{xz} = 7.372 \times 10^{16}, M_{yz} = -1.0965 \times 10^{17}, M_{xy} = 4.156 \times 10^{16} \end{bmatrix}$$

337   (16)

$$E2:\begin{bmatrix} M_{xx} = -1.064 \times 10^{18}, M_{yy} = -7.607 \times 10^{17}, M_{zz} = 1.8247 \times 10^{18} \\ M_{xz} = 3.141 \times 10^{17}, M_{yz} = 3.155 \times 10^{17}, M_{xy} = 1.114 \times 10^{18} \end{bmatrix}$$

338   To isolate source-related nonlinearity, we simulate both earthquakes adopting the a

339   simplified laterally homogeneous crustal model based on CRUST1.0 (Laske et al.,

340   2013), with physical properties and simulation parameters listed in Tables 2 and 3.

341   Free-surface condition is used at the top, and perfectly matched layer (PML)

342   condition is used on other boundaries, with 10-order differential accuracy in space.

343   **Table 2.** Physical properties of layered media.

Layer	Thickness (km)	vp (km/s)	vs (km/s)	ρ (kg/m³)
1	0.50	2.50	1.07	2.11
2	10.12	5.80	3.40	2.63
3	9.81	6.30	3.62	2.74
4	9.82	6.90	3.94	2.92
5	-	7.70	4.29	3.17

344

Table 3 Simulation parameters

Iterm	Paremeter (E1, E2)
Dominant frequency	1 Hz, 0.5 Hz
Moment magnitude	Mw5.4, Mw6.1
Depth	15 km, 30 km
Grid spacing	1 km, 2 km
Time step	5 ms, 2 ms
Source mechanisms	Eqs. (16)
Spatial differential accuracy	10th order

345

346   Fig. 11a presents the simulated 6C seismic records for E1 in radial (R),

347   transverse (T), and vertical (Z) coordinates, demonstrating prominent amplitude

348   predominance in the trans.Z and rot.T components. Nonlinear effects manifest as

349   subtle RMS amplitude changes (<1%), with rotational anomalies weaker than

350   translational counterparts (Fig. 11b). Normalized time-frequency spectral differences

351   further highlight distinct nonlinear patterns across components and wave phases:

352   direct and reflected waves show larger RMS amplitude changes in trans.R and Z

353   components, while surface waves in trans.T component display the strongest

354   nonlinear sensitivity. S-waves in rot.R and T components and surface waves in rot.Z

355   component show enhanced nonlinear effects, and Love-wave nonlinear perturbations

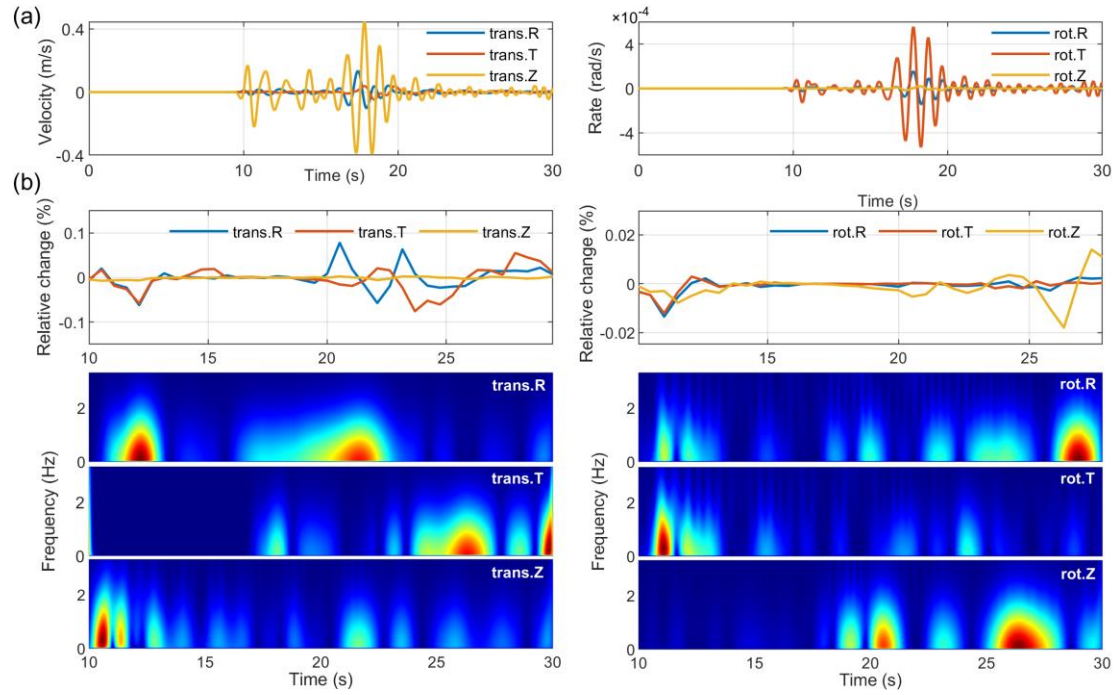356   in rot.Z component remain relatively weak.

Figure 11. (a) Synthetic 6C seismic records under linear condition, and (b) relative changes in RMS amplitude and nonlinear-induced time-frequency spectral difference for E1.

The larger-magnitude E2 simulation demonstrates stronger nonlinear effects, particularly in trans.Z and rot.T components (Fig. 12). Rayleigh waves show pronounced nonlinear distortions, while P-waves in trans.Z and surface waves in trans.R and T components exhibit moderate changes. S-waves and surface waves in the rot.R component are also affected, though rot.Z waveforms display minimal nonlinear alterations.
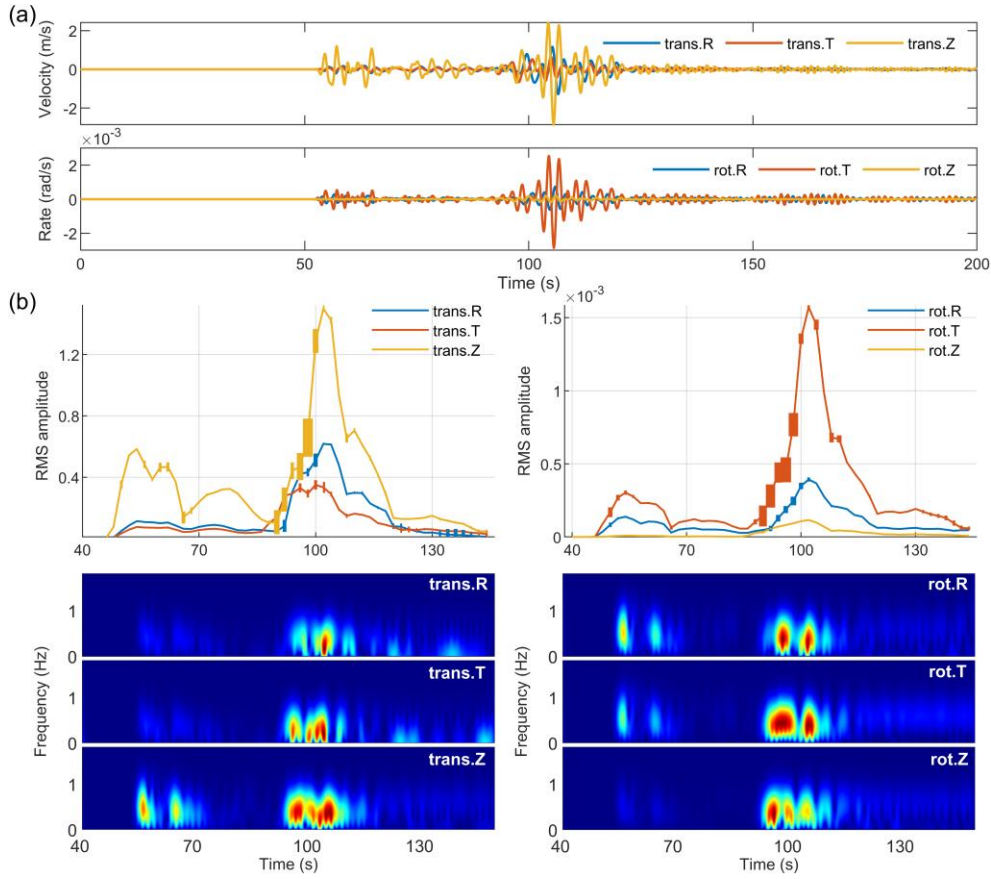
Figure 12. (a) Synthetic 6C seismic records under linear condition, and (b) RMS amplitude and nonlinear-induced time-frequency spectral difference for E2.

The simulations of E1 and E2 reveal some observational implications. For E1, the weak nonlinear effects (<1% amplitude changes) suggest that its receiver location may lie in a region of suppressed nonlinear coupling, likely due to unfavorable source-receiver geometry. In contrast, E2 exhibits stronger nonlinear signatures, particularly in surface waves. This enhanced nonlinear sensitivity in surface waves arises from their inherent P-S interference characteristics, making it a more viable candidate for studying nonlinear effects.

While rotational Z-component Love waves show minor nonlinear alterations, the translational R/T and rotational R/T components demonstrate more significant

381 changes, particularly in Rayleigh waves. These findings emphasize the need to

382 prioritize specific wave phases and components in future observational data studies.

383 For practical applications, wavefield separation techniques may be necessary to

384 isolate S-waves and surface waves in translational and rotational components, where

385 nonlinear effects are most pronounced.

386 **5 Discussion**

387 The incorporation of Green strain tensor-based nonlinearity into classical

388 elastodynamic theory introduces higher-order displacement gradient terms (Eqs. (7)

389 and (9)), fundamentally altering seismic wave dynamics by coupling volumetric and

390 shear deformation modes. In linear elasticity theory, volumetric (principal) and shear

391 strains are completely decoupled, and P-wave and S-wave are driven by normal

392 stresses and shear stresses, respectively. While ISO source simulation reveals P-S

393 wave conversion through nonlinear dilatational-shear interactions, the real-world

394 manifestation of such phenomena is constrained by multi-factor geological

395 complexities absent in our idealized models. Future work should prioritize

396 simulations incorporating velocity gradients and attenuation profiles to quantify how

397 propagation paths modulate nonlinear effects, particularly for surface waves where

398 site amplification may enhance nonlinear coupling.

399 The differences between E1 and E2 simulations further highlight the need to

400 explore complex source characteristics. While E2's larger magnitude produced clearer

401 nonlinear signatures, most natural earthquakes involve composite rupture dynamics

402 and asymmetric moment tensors. Expanding simulations to include finite-fault

403   sources and spatially varying rupture kinematics could reveal how source complexity

404   interacts with nonlinear strain accumulation.

405   Finally, while rotational components show theoretical sensitivity to nonlinear

406   effects, their practical utility remains constrained by observational challenges. Field

407   rotational motions are inherently weaker than translations, and current instruments

408   struggle to resolve most nonlinear changes. Addressing these limitations will require

409   coordinated advances in sensor technology, wavefield separation methods, and

410   targeted field observations focusing on moderate-strong earthquakes where nonlinear

411   effects may cross detection thresholds.

412   **6 Conclusions**

413   This work establishes a theoretical and numerical framework for analyzing

414   nonlinear seismic wave propagation through Green strain tensor strain tensor

415   formulations. Numerical simulations of three fundamental seismic moment tensor

416   sources (ISO, CLVD, DC) and two moderate-to-strong magnitude earthquakes yield

417   the following key conclusions.

418   (i) Force-source-type dependency: The spatial distribution is intrinsically tied to

419   source kinematics. ISO sources generate overall uniform nonlinear anomalies through

420   volumetric-shear coupling, CLVD sources amplify directional anomalies along

421   principal strain axes of compression/expansion, and DC sources restrict localized

422   nonlinearity to fault-aligned force couple orientations. These patterns arise from how

423   each force source geometry interacts with the nonlinear strain tensor.

424   (ii) Magnitude-energy relationship: Nonlinear effects scale exponentially with

425 seismic moment, becoming observationally significant for magnitudes above Mw5. At

426 Mw7, rotational components exhibit over 20% relative changes compared to linear

427 predictions, whereas changes remain negligible for Mw <4 events. This underscores

428 the importance of strain amplitude in triggering detectable nonlinear coupling.

429   (iii) Rotational motion sensitivity: Rotational components generally demonstrate

430 higher nonlinear sensitivity than translational components. Their practical

431 detectability depends on source-receiver azimuth.

432   (iiii) Wave-type specificity: Surface waves exhibit stronger nonlinear signatures

433 than body waves in both earthquake simulations, likely due to their inherent P-S

434 interference during propagation. However, current models inadequately address

435 surface wave nonlinearity, suggesting unresolved interactions between nonlinear

436 effects and site amplification.

437

438 **Author contributions.** WL: conceptualization, methodology, investigation, formal

439 analysis, writing - original draft. YW: conceptualization, writing - original draft and

440 revised draft. CC: investigation, formal analysis. LS: methodology.

441

442 **Data availability.** All data is simulated and available upon reasonable request.

443

444 **Competing interests.** The contact author has declared that neither of the authors has

445 any competing interests.

446

447 **Disclaimer.** Publisher's note: Copernicus Publications remains neutral with regard to

448 jurisdictional claims made in the text, published maps, institutional affiliations, or any

449 other geographical representation in this paper.

450

453

454 **References**

455 Aki, K., and P. G. Richards. Quantitative seismology, 2nd ed, California: University

456   Science Books, https://doi.org/10.1029/2003EO210008, 2002.

457 Bataille, K., Contreras, M.: Nonlinear elastic effects on permanent deformation due to

458   large earthquakes, Phys. Earth Planet. Inter., 175(1), 47-52,

459   https://doi.org/10.1016/j.pepi.2008.02.016, 2009.

460 Bernauer, M., Fichtner, A., and Igel, H.: Reducing nonuniqueness in finite source

461   inversion using rotational ground motions, J. Geophys. Res.-Solid Earth, 119(6),

462   4860-4875, https://doi.org/10.1002/2014JB011042, 2014.

463 Chen, C., Wang, Y., Sun, L. X., Lin, C. J., Wei, Y. x., Liao, C. Q., Lin, B. H.,and Qin,

464   L. P.: Six-component earthquake synchronous observations across Taiwan Strait:

465   Phase velocity and source location, Earth and Space Science, 10,

466   e2023EA003040, https://doi.org/10.1029/2023EA003040, 2023.

467 Chen, Q. J., Yin, J. E., and Yang, Y. S.: Time-frequency characteristic analysis of

468   six-degree-freedom ground motion records, Chinese Quarterly of Mechanics, 35,

469   (3),   499-506,

470   https://link.oversea.cnki.net/doi/10.15959/j.cnki.0254-0053.2014.03.033,   2014

471   (in Chinese).

472   Dong, L. G., and Ma, Z. T.: A staggered-grid high-order difference method of

473   one-order elastic wave equation, Chinese J. Geophys., 43(3), 411-419, 2000 (in

474   Chinese).

475   Donner, S., Bernauer, M., and Igel, H.: Inversion for seismic moment tensors

476   combining translational and rotational ground motions, Geophys. J. Int., 207(1),

477   562-570, https://doi.org/10.1093/gji/ggw298, 2016.

478   Feng, X., Fehler, M., Brown, S., Szabo, T. L., and Burns, D.: Short-period nonlinear

479   viscoelastic memory of rocks revealed by copropagating longitudinal acoustic

480   waves, J. Geophys. Res.-Solid Earth, 123(5), 3993–4006,

481   https://doi.org/10.1029/2017JB015012, 2018.

482   Graizer, V. M.: Strong motion recordings and residual displacements: what are we

483   actually recording in strong motion seismology? Seismol. Res. Lett., 8(4),

484   635-639, https://doi.org/10.1785/gssrl.81.4.635, 2010.

485   Graizer, V. M.: Inertial seismometry methods, Earth Physics, 27(1), 51-61, 1991.

486   Graves, R. W.: Simulating seismic wave propagation in 3D elastic media using

487   staggered-frid finite differences, Bull. Seismol. Soc. Am., 86(4), 1091-1106,

488   1996.

489   Gilbert, F.: Excitation of the normal modes of the Earth by earthquake sources,

490   Geophys. J. R. astr. Soc, 22(2), 223-226,

491   https://doi.org/10.1111/j.1365-246X.1971.tb03593.x, 1970.

492   Guyer, R. A., and Johnson, P. A.: Nonlinear mesoscopic elasticity: evidence for a new

493   class of materials, Physics Today, 52(4), 30-36, https://doi.org/10.1063/1.882648,

494   1999.

495   Hua, S. B., and Zhang, Y.: Numerical experiments of moment tensor inversion with

496   rotational ground motions, Chinese J. Geophys., 65(1), 197-213,

497   https://doi.org/10.6038/cjg2022P0668, 2022 (in Chinese).

498   Huras, L., Zembaty, Z., Bonkowski, P. A., and Bobraet, P.: Quantifying local stiffness

499   loss in beams using rotation rate sensors, Mech. Syst. Signal Proc., 151, 107396,

500   https://doi.org/10.1016/j.ymssp.2020.107396, 2021.

501   Ichinose, G. A., Ford, S. R., and Mellors, R. J.: Regional moment tensor inversion

502   using rotational observations, J. Geophys. Res.-Solid Earth, 126(2),

503   e2020JB020827, https://doi.org/10.1029/2020JB020827, 2021.

504   Jia, L., Yan, S. G., Zhang, B. X., and Huang, J.: Research on perturbation method for

505   nonlinear elastic waves, J. Acoust. Soc. Am., 148, EL289–EL294,

506   https://doi.org/10.1121/10.0001980, 2020.

507   Jost, M. L., and Hermann, R. B.: A students guide to and review of moment tensors,

508   Seism. Res. Lett., 60, 37-57, https://doi.org/10.1785/gssrl.60.2.37, 1989.

509   Knopoff, L., and Randall M. J.: The compensated linear-vector dipole: A possible

510   mechanism for deep earthquakes, J. Geophy. Res., 75(26), 4957–4963,

511   https://doi.org/10.1029/JB075i026p04957, 1970.

512   Kozak, J. T.: Tutorial on earthquake rotational effects: historical examples, Bull.

Seismol. Soc. Am., 99(2B), 998-1010, https://doi.org/10.1785/0120080308, 2009.

Laske, G., Masters, G., Ma, Z. T., and Pasyanos, M.: Update on CRUST1. 0-A 1-degree global model of Earth's crust, EGU General Assembly 2013, 15, EGU2013-2658, 2013.

Lee, C. E. B., Celebi, M., Todorovska, M. I., and Diggles, M. F.: Rotational seismology and engineering applications — Proceedings for the First International Workshop, Menlo Park, California, U.S.A.—September 18 to 19, 2007: U.S. Geological Survey Open-File Report 2007-1144, 46 p. http://pubs.usgs.gov/of/2007/1144/, 2007.

Li, H. N.: Study on rotational components of ground motion, Journal of Shenyang Architectural and Civil Engineering Institute, 7(1), 88-93, 1991 (in Chinese).

Li, H. N., and Sun, L. Y.: Rotational components of earthquake ground motions derived from surface waves, Earthq. Eng. Eng. Vib., 21(1), 15-23, https://link.oversea.cnki.net/doi/10.13197/j.eeev.2001.01.003, 2001 (in Chinese).

Madariaga, R.: Dynamics of an expanding circular fault, Bull. Seismol. Soc. Am., 66(3), 639-666, https://doi.org/10.1007/BF02246368, 1976.

McCall, K. R.: Theoretical study of nonlinear elastic wave propagation, J. Geophys. Res., 99(B2), 2591-2600, https://doi.org/10.1029/93JB02974, 1994.

Moczo, P., Robertsson, O. J., and Eisner, L.:The finite-difference time-domain method for modeling of seismic wave propagation, Advances in Geophysics, 48, 421-516. https://doi.org/10.1016/S0065-2687(06)48008-0, 2007.

535   Oliveira, C. S., and Bolt, B. A.: Rotational components of surface strong ground

536   motion, Earthq. Eng. Struct. D. 18(4), 517–526,

537   https://doi.org/10.1002/eqe.4290180406, 1989.

538   Pei, Z. L.: Numerical simulation of elastic wave equation in 3-D anisotropic media

539   with staggered-grid high-order difference method, Geophysical Prospecting for

540   Petroleum, 44(4), 308-315, https://doi.org/10.3969/j.issn.1000-1441.2005.04.002,

541   2005 (in Chinese).

542   Renaud, G., Le Bas, P. Y., and Johnson, P. A.: Revealing highly complex elastic

543   nonlinear (anelastic) behavior of Earth materials applying a new probe: Dynamic

544   acoustoelastic testing, J, Geophys. Res.-Solid Earth, 117, B06202, ,

545   https://doi.org/10.1029/2011JB009127, 2012.

546   Renaud, G., Rivière, J., Le Bas, P. Y., and Johnson, P. A.: Hysteretic nonlinear

547   elasticity of Berea sandstone at low-vibrational strain revealed by dynamic

548   acoustoelastic testing, Geophys. Res. Lett., 40(4), 715-719,

549   https://doi.org/10.1002/grl.50150, 2013.

550   Sun, L., Yu, Y., Lin, J. Q., and Liu, J. L.: Study on seismic rotation effect of simply

551   supported skew girder bridge, Earthquake Engineering and Engineering

552   Dynamics, 37(4), 121-128, https://doi.org/10.13197/j.eeev.2017.04.121.sunl.014,

553   2017 (in Chinese).

554   Sun, L. X., Zhang, Z., and Wang, Y.: Six-component elastic-wave simulation and

555   analysis, EGU General Assembly 2018, Geophysical Research Abstracts, 20,

556   EGU2018-14930-1, 2018.

557   TenCate, J. A., Malcolm, A. E., Feng, X., and Fehler, M. C.: The effect of crack

558   orientation on the nonlinear interaction of a P wave with an S wave, Geophys.

559   Res. Lett., 43(12), 6146-6152, https://doi.org/10.1002/2016GL069219, 2016.

560   Virieux, J.: P-SV wave propagation in heterogeneous media; velocity-stress

561   finite-difference   method,   Geophysics,   51(4),   889-901,

562   https://doi.org/10.1190/1.1442147, 1986.

563   Wang, L., Luo, Y. H., and Xu, Y. H.: Numerical investigation of Rayleigh-wave

564   propagation   on   topography   surface,   J.   Appl.   Geophys.,   86,   88–97,

565   https://doi.org/10.1016/j.jappgeo.2012.08.001, 2012.

566   Wessel, P., Luis, J. F., Uieda, L., Scharroo, R., Wobbe, F., Smith, W. H. F., and Tian,

567   D.:   The   generic   mapping   tools   version   6,   Geochemistry,   Geophysics,

568   Geosystems, 20, 5556–5564, https://doi.org/10.1029/2019GC008515, 2019.

569   Xu, Y. X., Xia, J. H., and Miller, R. D.: Numerical investigation of implementation of

570   airearth boundary by acoustic-elastic boundary approach, Geophysics, 72 (5),

571   SM147–SM153, https://doi.org/10.1190/1.2753831, 2007.

572   Yan, Y. Y.: Seismic response analysis of high-rise building under different types of

573   multi-dimensional earthquake ground motions (Ph.D. dissertation), Jiangsu

574   University, 2017(in Chinese).

575   Yu, S. B., Kuo, L. C., and Punongbayan, R. S., Emmanuel, G.R.: GPS observation of

576   crustal deformation in Taiwan-Luzon region, Geophys. Res. Lett., 26(7), 923-926,

577   https://doi.org/10.1029/1999GL900148, 1999.

578   Yang, D. H., Liu, E., Zhang, Z.J., and Teng, J.: Finite-difference modelling in

579   two-dimensional anisotropic media using a flux-corrected transport technique,

580   Geophys.   J.   Int.,   148(2),   320–328,

581   https://doi.org/10.1046/j.0956-540x.2001.01575.x, 2002.

582   Zheng, H. S., Z. J. Zhang, and Liu, E. R.: Nonlinear seismic wave propagation in

583   anisotropic media using the flux-corrected transport technique, Geophys. J. Int.,

584   165(3), 943-956, https://doi.org/10.1111/j.1365-246X.2006.02966.x, 2006.

585   Zhou, C., Zeng, X. Z., Wang, Q. L., and Liu, W. Y., and Wang, C. Z.: Rotational

586   motions of the Ms7.0 Jiuzhaigou earthquake with ground tilt data, Science China

587   Earth Science, 62(5), 832-842, https://doi.org/10.1007/s11430-018-9320-3, 2019.